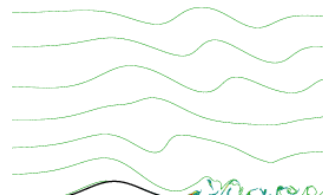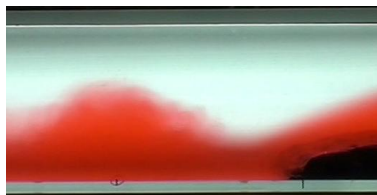# Modelling the Föhn in the MIM Laboratory

A thesis submitted for the degree of Bachelor of Science
Chair of Theoretical Meteorology
Department of Physics
Ludwigs Maximilians University Munich

Josef Schröttle, 20. August 2010

Declaration

I confirm that this is my own work and the use of all material from other sources has been properly and fully acknowledged.

Josef Schröttle

Acknowledgements

To my grandpa, who showed me the Föhn for the first time,
*while we were climbing the Alps in the winter.*

Contents

1. Introduction

„If the earth were greatly reduced in size, while maintaining its shape,
*it would be smoother than a billiard ball!" (Ronald B. Smith, 1979)*

Föhn in the Alps, Bora at the Mediterranean and Chinook in the Rocky Mountains are all downslope winds of major mountain chains responsible for local temperature changes, cloud formation, and rain. Field studies (Mayr 2004, 2006, 2008) like the Mesoscale Alpine Program (MAP 1999), numerical models (Smith 2005, Durran 2002), and laboratory experiments (Etling 2010) in the last ten years have emphasized the importance of mountains on the planet's weather. For high school and university students the question remains: Why do mountains, small in size compared to the planet's radius, have such a great influence on the weather and how do mountains affect the atmospheric circulation?

A weather map of Europe for a typical Föhn day in southern Germany is shown in Fig. 1.1. A low pressure system over Spain and France creates an anticlockwise circulation. Air is forced to flow from northern Italy to Germany over the Alps. Air temperature is more than 5 degrees warmer in southern Germany than in Italy. On the windward side of the Alps convective clouds and rain develop (Fig. 1.2). The northward wind creates higher pressure on the windward side, which is visible on a synoptic scale by isobar deformation, the so called **Föhn nose** (Fig. 1.3). These are characteristic synoptic conditions for alpine Föhn (Goler 2009).

The goal of this thesis is to explain the design and implementation of a Föhn experiment which can be performed in the MIM laboratory for teaching purposes. First of all, various Föhn theories are summarized in Chapter two. An experiment for students in the laboratory will be described in Chapter 3, which demonstrates the typical Föhn features, and the results presented in Chapter 4. Furthermore, a more complex experiment a little bit closer to what is observed in the atmosphere will be set up and observed in Chapter 5. Finally, a numerical model will be introduced in Chapter 6 for students to do their own simulations.
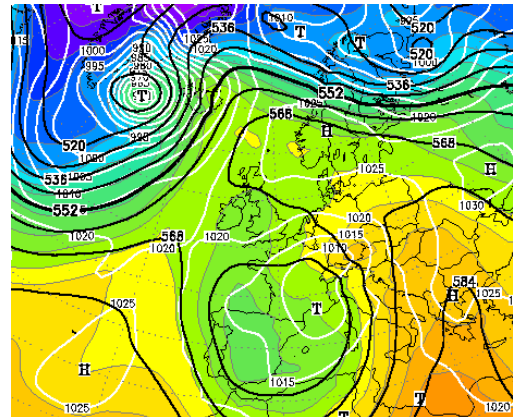
Fig. 1.1: Synoptic situation over Europe during a Föhn event in the Alps on Nov. 5th 2008 from wetter3.de. Black lines show the height of the 500hPa pressure surface. White lines show pressure at sea level and the shading shows thickness between the 1000hPa and 500hPa level, depending on temperature.
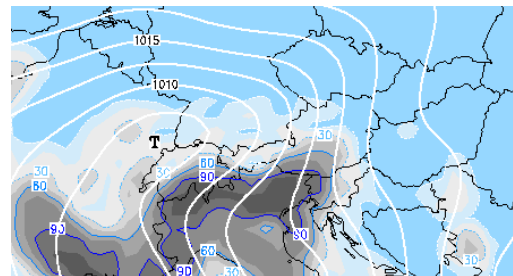
Fig. 1.2: Thickness of the lower cloud layer – indicating cloudy sky over northern Italy.
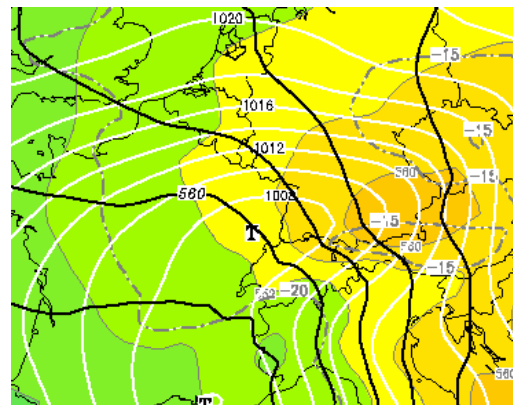
Fig. 1.3: Föhn Nose – isobar deformation in lee (north) of the Alps.

2. Mountain Wave Theory

A number of Föhn theories have been described by Steinacker (2006) and are outlined here. All schematics on the right are from the coresponding article by Steinacker.

In mountain meteorology of the 19th century an interesting phenomenon in the Alps during the winter months was a sudden rise in temperature together with strong downslope winds. Initially this observation was explained by the advection of warm air. Hann (1866) however introduced the **thermodynamic Föhn theory** (Fig. 2.1a) for the Alps, which was accepted, after observing the Föhn in Greenland. This theory explained the warming in lee of the mountains as ascending air on the windward side of the mountain being forced to rise and condense, cooling at the moist-adiabatic laps rate, and subsequently sinking on the lee side of the mountain and warming at the larger dry-adiabatic lapse rate. On the windward side the condensed water falls out as rain. Diabatic effects, such as radiation, evaporation and condensation are studied further.

In Switzerland rain and high clouds were common on the windward side, while in Austria 50% of the observed Föhn cases could occur without any rain at all (Seibert 1990). Consequently the air must not always rise on the windward side (Fig. 2.1b).

One question regarding these theories was how the warm air from above can replace the heavier cold air on the ground as it descends. Therefore, Steiff-Becker developed a so called **vertical aspiration theory** in 1931, which states that warmer air moves downwards by eroding the cold air on the ground from above (Fig. 2.2a).

A synoptic approach towards cold air aspiration was proposed by Ficker, also in 1931. He introduced the **horizontal aspiration theory** (Fig. 2.2b). The cold air is removed here by a low pressure area at the surface which moves closer to the mountain. The cold air is forced to flow away from the mountain towards the low pressure area. Later on various **Föhn features** were studied. Gravity waves can form behind a mountain when air flows over it, and can be observed in the
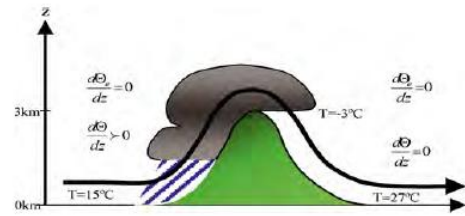

Fig. 2.1a: Classical thermodynamic model: Adiabatic cooling of the uprising air, condensation and rainfall on the windward side. Adiabatic warming and evaporation on the lee side of the mountain.

Fig. 2.1b: Here the air does not rise but only descends from greater height. No clouds form on the windward side.

Fig. 2.2a: In order that the warm air reaches the ground it erodes the lower colder layer of air from the top down as it drifts away. The rotating arrows indicate the turbulence on the surface of the colder layer.

Fig. 2.2b: Here the colder layer on the ground is aspirated horizontally from a low pressure area.

potential temperature contours (Fig. 2.3.a). A wavelength of 5-10 km is indicated for the mountain with a height of 3 km here. These *lee waves*, a mesoscale phenomenon were first discovered above the Hirschtal, a valley in Silesia, in 1933 by Hirth a popular glider pilot (Dörnbrack 2006). He looked closely at a well known lenticular cloud above the Hirschtal and wondered why it did not move, despite the strong winds. Hirth's observations lead to new concepts in mountain meteorology. After collectin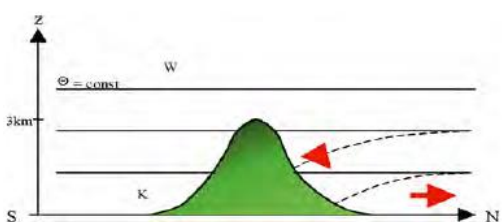g data from a glider flight tournament in the Riesengebirge, a German mountain Range, Küttner published about the development of *mountain waves* due to buoyancy oscillations (Küttner 1938, see below). Such oscillations allow the gliders to rise to high altitudes (Dörnbrack 2006).

The presence of *lenticular clouds* indicates Föhn activity. The cloud forms in the cusp of a *gravity wave* when the air is lifted up. Several lenticular clouds can follow behind each other or can be stacked on top of each other. Figure 2.3b was taken by a friend in Austria on a Föhn day and shows a lenticular cloud. The formation of a lenticular cloud requires that sufficient moisture is present so that the lifted air parcels can condense. Gravity waves in the atmosphere (Fig. 2.3c) can extend horizontally over a few hundred kilometers (Baines 1995). The forced oscillation of an air parcel as it rises over the mountain is analogous to a swinging pendulum as a damped oscillator. As the air rises, it cools adiabatically, becomes colder and heavier than the environment in a stably stratified atmosphere. As it descends, the opposite effect takes place: the air parcel warms adiabatically and becomes warmer than its environment. As a consequence it rises again and the process repeats until it is fully damped. These up and down oscillations are called *buoyancy oscillations* (Meted 2004).

In 1944 Frey introduced as driving mechanism of the Föhn a *solenoid field* which develops (Fig. 4) in the mountain area, when the pressure gradient forces the air to flow over the mountain (Frey, 1944). Isobars and Isotherms cross and cause baroclininc instability, which generates a solenoid
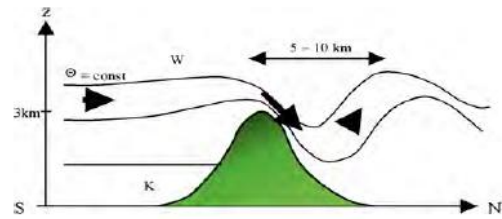
Fig. 2.3a: The isentropes are slightly tilt due to blocking on the windward side and form lee waves.

Fig. 2.3b: Lenticular Cloud above Stubai Valley – Sebastian Müller.

Fig. 2.3c: A series of cloud lines due to gravity waves – metvuw.com.
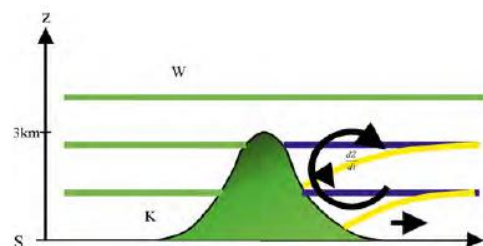
Fig. 2.4: Isobars and Iseotherms form a solenoid field. The air is rotating.

Fig. 2.5a: Cloud wall expanding to the lee side of the mountain. The arrow indicates rapid descend of cold air from the cap cloud.

field and moves the warm air to the ground (Frey, 1944). Synoptic scale variations of the temperature field can furthermore explain sudden Föhn intermissions (Frey, 1953).

Blocking or partial blocking leads to a deep, cold pool of air upstream of the barrier. As air rises, clouds form and huge wall cap clouds (Mayr 2006) expand over the mountain top. A cloud wall visible from the lee side is the basis for Roßman's **waterfall theory** from 1950. He suggests that the air in the cloud cap is colder compared to its environment and sinks rapidly (Fig. 2.5a). On its descent it warms adiabatically, the cloud water evaporates and the cloud dissolves (Fig. 2.5b).

Many of the mesoscale observations mentioned so far can be explained with the **hydraulic model**. In this theory Schweizer (1953) compares the atmosphere to a shallow water system consisting of a single or several layers. In the atmosphere the homogeneous layers are determined by constant potential temperature and separated by an inversion (Mayr 2006).

The **hydraulic model** includes features such as **cap clouds**, **hydraulic jumps**, **lee waves** and **rotors**, which have been thoroughly investigated during the Mesoscale Alpine Program (MAP). In recent years considerable research has been published and observations have been compared with numerical studies and laboratory experiments (Smith 2005, Durran 2002, Mayr 2004 and Dörnbrack 2006). A good summary of the concept and features can be found in the Meted Program from UCAR: "Mountain Waves and Downslope Winds" (2004).

A **hydraulic jump** (Fig. 2.6a), also referred to as **turbulent bore**, can occur in the atmosphere, oceans and rivers. It is caused by rapid energy transformation from potential to kinetic energy of the fluid parcel or vice versa. During this discontinuous process, some energy dissipates into turbulence (Simpson 1997). For continuous transfer the result is an **undular bore**, referred to as gravity wave (Fig. 2.3a) in the atmosphere and the energy travels with the wave.

Fig. 2.5b: Cap cloud of a fjord in Norway – Axel Hennig.
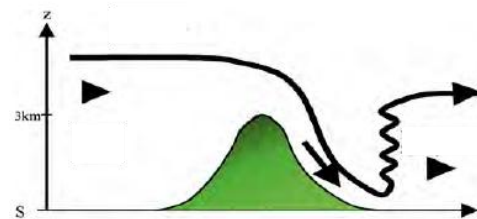
Fig. 2.6a: Cold air on the ground and warm air above descending rapidly on the lee side lead to a hydraulic jump.
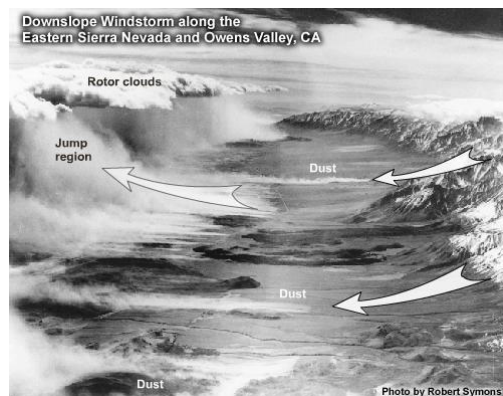
Fig. 2.6b: Hydraulic jump – photographed in 1950 in the Sierra Nevada. In the jump region sand is lifted up and rotor clouds form.

Fig. 2.6c: Surfer's wave – a hydraulic jump in the Eisbach a river in the English Garden in Munich – münchen.de.

The **hydraulic jump** observed in the Sierra Nevada (Fig. 2.6b) in March 1950 by Robert Symons shows dust rising left, downstream of the mountain range. After air flows over the mountain it descends very quickly. In the jump region it rises up again in a turbulent way. Clouds develop due to the uprising air, which reaches a saturated level and water condenses. A special type of cloud that forms in the jump region with a vortex structure is the **Rotor cloud**. Below a gravity wave, rotors can develop also even in a clear sky, which can be hazardous to pilots (Dörnbrack 2006). Although, wind speeds can be very high, for air traversing the mountain, the cloud is stationary – since the wave on which the cloud forms is stationary. An example of a hydraulic jump which can be regularly seen in Munich is the surfer's wave in the Eisbach in the English Garden (Fig. 2.6c).

This work will focus on the hydraulic model of the Föhn, which explains features like hydraulic jumps and lee waves. These features are fundamental for cloud formation in the mountains. By concentrating on the hydraulic features of the Föhn, it is possible to investigate airflow over mountains in the meteorological laboratory here in Munich.

3. Experiment Construction for a Single Layer

The Meteorology Laboratory of the Ludwigs Maximilians University in Munich has a tank for gravity current experiments (Fig. 3.1) with dimensions 250 cm long, 25 cm wide, and 25 cm high. In this tank flow relative to an obstacle can be generated by pulling the obstacle through the tank (Chapter 4) and the subsequently developing waves observed. In the case of a wave length λ >> water depth H the experiment is an example for a typical shallow water system (Erhardt 2007), which can be comparable to the atmosphere (Schweitzer 1953) under certain conditions explained in the following section.

*Fig. 3.1: Schematic of the gravity current tank in the Meteorology Laboratory in Munich.*

3.1   Similarity Rules

In order to compare model experiments in the laboratory with observations of the Föhn in the atmosphere it is crucial to have similar forces acting (Cohen 2008). As water is used instead of air, the forces working on a water parcel need to be compared to the forces working on air parcels in the atmosphere. Both phenomena can be described with basic hydrodynamic equations such as the Continuity (Eq. 3.1), Bernoulli (Eq. 3.2), Euler (Eq. 3.3) and Navier Stokes Equation (Eq. 3.4) with velocity vector $\vec{v}$, pressure p, fluid height h, orography profile e, maximum mountain height h_m, density ρ, kinematic viscosity ν, coriolis parameter f, length scale L, average velocity V, undisturbed fluid height H far away from the mountain, and gravity g.

The forces present are pressure gradient, friction, Coriolis, and gravity force. With these forces as non linear terms in the equation, it is not enough to downscale the problem linearly in every variable. Dimensional analysis of the basic equations is necessary, which leads to the non dimensional numbers such as the **Reynolds**, **Rossby**, and **Froude numbers** (Tab. 3.1). They represent a relationship between the forces acting in the experiment. Of special importance in these experiments is the restoring force, which is the gravity force. For the two layer experiment in Chapter 5, the reduced gravity force will act, as in the earth's atmosphere, when an inversion separates two layers of different temperature (Smith 2005).

Shallow water Equations			Nondimensional Numbers	
Continuity	$\dfrac{\partial h}{\partial t} + \nabla \cdot (\vec{v}h) = 0$	(Eq. 3.1)	Froudenumber	$F = \dfrac{V}{\sqrt{gH}}$
Bernoulli	$p + \rho\dfrac{v^2}{2} + \rho g(h+e) \equiv const$	(Eq. 3.2)	Reynolds number	$Re = \dfrac{VL}{\nu}$
Euler	$\dfrac{D\vec{v}}{Dt} = -\dfrac{1}{\rho}\nabla p - g - f \times \vec{v}$	(Eq. 3.3)		
Navier Stokes	$\dfrac{D\vec{v}}{Dt} = -\dfrac{1}{\rho}\nabla p - g - f \times \vec{v} + \nu\Delta\vec{v}$	(Eq. 3.4)	Rossby number	$Ro = \dfrac{V}{fL}$

To analyze the Föhn experiments, the important non dimensional number is the Froude number (Baines 1987, 1995). As in the diagrams presented by Baines, it will be used to identify the flow regime (Chapter 5) and compare atmospheric observations with the laboratory experiments in single layer models as well as two layer models (Chapter 6). The Froude number is usually introduced as a ratio between the velocity a fluid parcel and the shallow water wave speed (Landau & Lifshitz 1987, Cohen 2008). In the laboratory, the parameters of the Froude number describe fluid velocity, gravitational acceleration, and water depth. In nature, the variables are typical wind speed, buoyancy, and height of the observed potential temperature surface (Chapter 2).
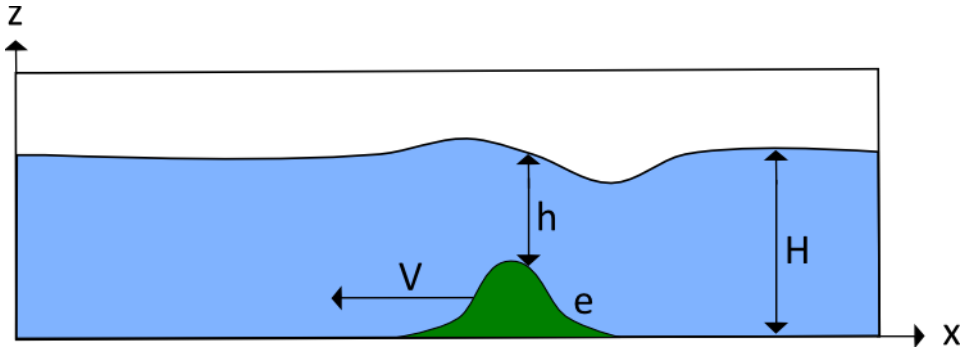
Fig. 4.1: Schematic of the single layer experiment with profile of the orography e, water depth h, pulling velocity V and water depth $h_\infty=H$ far away from the obstacle and maximum mountain height h_m.

Not all non dimensional variables can coincide between laboratory experiment and natural observation. Thus only an optimization is possible here. The Reynolds number is a measure for turbulence (Cohen 2008). In the atmosphere it is six dimensions bigger than in the laboratory experiment (Tab. 3.1), which means that the flow in the gravity current tank is more laminar than in nature. This offers the possibility to study the laminar flow more closely and to understand it better before including turbulent effects in the students experiment (Chapter 7). Furthermore, the Reynolds number measures the ratio between acceleration and viscous effects. In the laboratory and in nature, acceleration is several magnitudes larger than viscous forces.

The coriolis force is only one dimension smaller compared to acceleration for single mountains in the Alps with a wind speed of 10 m/s and a mountain length of order 10 km and f=10^{-4} 1/s. For larger mountain ranges such as in Greenland the Coriolis force may not be neglected (Sprenger 2008). The presence of the Coriolis force would make the students experiment more complicated. Fortunately, laboratory environment is far away from being influenced by Coriolis force (Tab. 3.1). Thus, viscosity and the Coriolis force will be neglected in the experiments presented here.

		Alps	Laboratory
Rossby number	acceleration : coriolis force	10 > 1	1000 >> 1
Reynolds number	acceleration : friction	10^{10}	10^4

Table 3.1: Rossby and Reynolds number calculated for laboratory with 20°C and density of standard atmosphere.

For constructing obstacles with similar properties as real mountains, the obstacle height is important (Baines 1987), as well as the length scale described by the horizontal wave number of the obstacle (Smith 1979).

3.2   Mountain Shape
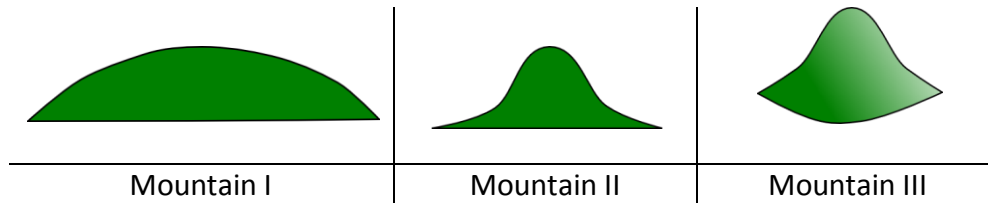
Table 3.2: Types of mountains used in the experiments. Mountains I and II are two-dimensional ridges, while mountain III is a three-dimensional cone.

Three different types of mountains were constructed (Tab. 3.2), beginning with a parabola shaped mountain (mountain I) similar to Long's experiment (1954), with dimensions 24.5 ± 0.1 cm long and 4.3 ± 0.1 cm high. It was deformed to a two-dimensional Gaussian shape mountain (mountain II), now 12.5 ± 0.1 cm long and 4.3 ± 0.1 cm high. A similar mountain has been used by Wedi (2003) and Durran (2002) for numerical studies. Finally a three-dimensional Gaussian cone was modeled (mountain III) with same dimensions as mountain II, but rotationally symmetric, similar to an idealized volcano such as Mount Fuji, where Föhn effects such as lenticular clouds have been observed (Baines 1995).
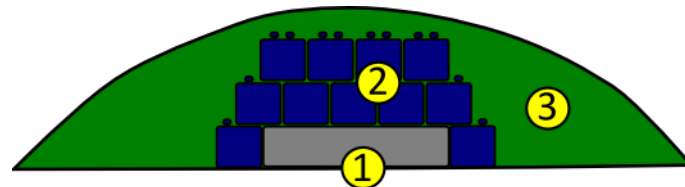
Fig. 3.2: Schematic slice through the parabola shaped mountain. (1) Metal weights, (2) Lego, and (3) Modeling clay.

The mountains were built using Lego (Fig. 3.2 - 2). Metal weights were included in the mountain (Fig. 3.2 - 1) to prevent the mountain from floating. To make the surface smooth modeling clay (Fig. 3.2 - 3) was spread on top of the mountains. It was crucial to leave a gap of 1 cm between the ends of mountain I and tank wall, so that water can flow besides the mountain and prevent an upstream accumulation of water when the mountain is pulled. For mountain II, the Gaussian ridge, more space was left on each side between the ends of the mountain and tank wall, so that the mountain was only 16 cm wide. To make the mountains move smoothly in the tank when they are pulled all mountains were set on a Lego plate with a width of 25 cm as wide as the tank.

3.3   Pulling Mechanism

To create a flow over the mountains (Fig. 3.3 - 1), similar to a wind over the Alps, they had to be pulled through the tank. A similar concept was used by Long (1954 and 1955). At first, a simple hand drill connected with kite string to the mountain was used to pull the mountain at a relatively constant speed through the water. The kite string (Fig. 3.3 - 2) was fixed inside

the mountain on a weight. Later on another string on the opposite side of the mountain was attached to allow the mountain to be pulled in each direction, and thus did not have to be taken out of the tank and returned to the starting end. As a result the water was disturbed less.
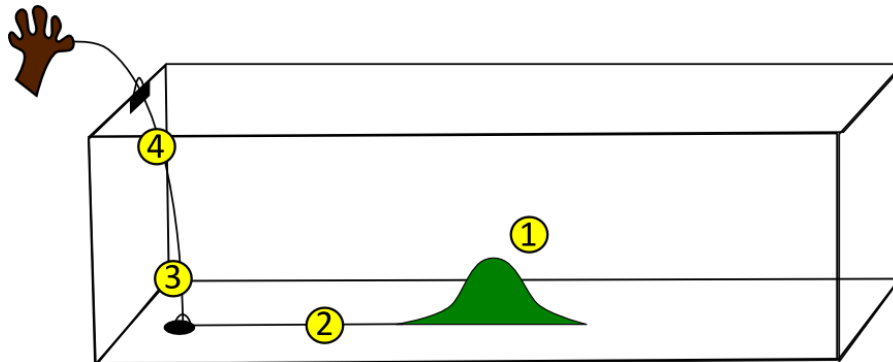
*Fig. 3.3: Schematic of the final pulling mechanism implemented inside the gravity current tank. (1) Mountain, (2) kite string, (3) suction cup with hook, and (4) guide.*

The hand drill was replaced by an electrical motor, where the speed could be regulated. Nevertheless the motor together with the mountain was very inertial and reacted only slowly when the speed was increased. In the end pulling the kite string by hand seemed the best way, as the speed could be increased quickly and a large range of velocities could be covered in one pull. Due to its ease, this last method seemed appropriate as the student pulling the mountain could also stand in front of the tank and view the flow.

A problem arose when the mountain was pulled to one end of the tank where it always lifted off the tank bottom due to the vertical component of the pulling force. To solve this problem, hooks attached to suction cups were fixed on both ends on the bottom of the tank. The kite string passed through the hooks (Fig. 3.3 - 3) and then through a guide (Fig. 3.3 - 4) at the edge of the tank and could be pulled by hand.

3.4   Video Documentation & Analysis
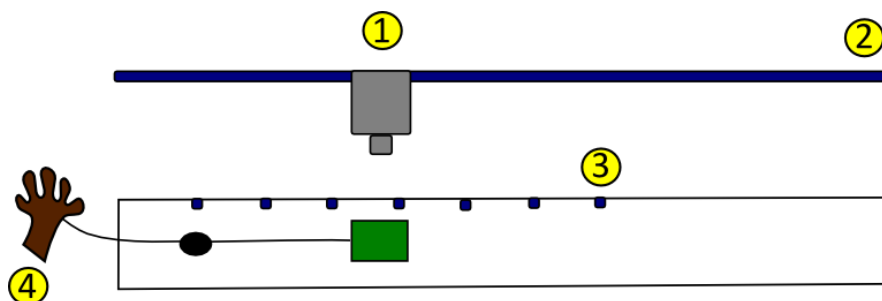
Fig. 3.4: Schematic of camera set up and gravity current tank from above. (1) Digital camcorder, (2) tripod movement, (3) markers, (4) mountain puller.

A number of different documentation methods were trialed. Several cameras helped to keep records of the stream patterns observed in the gravity current tank. Initially a small wireless camera was set on top of the hill and moved along the stream in order to get a stationary

image of the flow pattern in front of the hill. Unfortunately the quality of this camera was not sufficient.

Mostly used was a regular digital camcorder (Fig. 3.4 - 1) set on a tripod with wheels to allow the camera to be moved along the tank. To maintain a constant distance from the tank, a marker was placed on the floor about half a meter away from the tank (Fig. 3.4 - 2). The camera assistant moved the tripod with the same speed as the mountain was moved by the experimenter (Fig. 3.4 - 4), thus allowing a close up of the flow pattern to be recorded.

For complex topography, faster relative flows, or for smaller scale analysis, a slow motion camera recording at 300 frames per second was used. As mostly two dimensional flow patterns were analyzed the camera was also set on the tripod, focusing at right angles to the tank. To investigate more complex orography flows this camera could be placed at different angles relative to the tank.

The movies from the video camera were analyzed using "Kino" in Linux which proved to be very useful. It allowed frame-by-frame analysis, along with showing a scene in slow motion. The time interval was 400 ms, which is the difference between the single frames with a regular camcorder. From single frames it was possible to measure, for example, wave amplitude or distance from the mountain, based on reference markers (Fig. 3.4 - 3) by converting pixels to cm. The markers a length of 10.5 ± 0.1 cm and were set every 20 ± 0.1 cm to provide a basis for velocity measurements on the computer. The results were documented and analyzed with "Excel" tables (DVD). In the following Chapter typical atmospheric Föhn features (Chapter 2) were replicated in the MIM laboratory.

4. Laboratory Results for a Single Layer Model

The first step to model flow over an obstacle involved using a single layer of fluid. These experiments are based on a general theory of Peter Baines (1987 and 1995) who identified flow regimes of flow over an obstacle in a shallow water tank. Similar experiments have been conducted by Long (1953, 1954 and 1955) and just recently by Etling (2010). The flow patterns strongly depend on Froude number and mountain height relative to the water depth. To obtain a certain Föhn feature (Chapter 2) that is characteristic for the observed flow regime, water depth H and pulling velocity V are varied. Gravity waves (Section 4.1), hydraulic jumps downstream (Section 4.2) and upstream (Section 4.3), as well as, wave breaking (Section 4.4) are observed.

4.1   Gravity Waves

Gravity waves have an interesting structure in the atmosphere, visible when there are lenticular clouds (Chapter 2). Detailed studies in the Mesoscale Alpine Program described by Smith (1976, 2002 and 2005) motivate their investigation and understanding for students here in the laboratory.
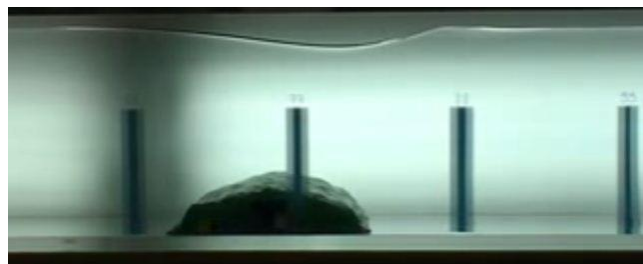
Fig. 4.1a: One wave cusp after 2.2 seconds as the mountain is accelerated towards the left.

Fig. 4.1b: Wave with two cusps after 2.6 seconds.

Fig. 4.1c: A wave train with several cusps forms after 3.2 seconds as the mountain approaches the left end of the tank.

To model gravity waves, mountain I (see Section 3.2) is used with a water depth of H = 17.5 ± 0.1 cm and an average pulling speed of V = 54 ± 1 cm/s. For this experiment the Froude number is F = 0.4, and the non dimensional mountain height is h_m/H = 0.3. The wave trough of the water surface above the mountain (Fig. 4.1a) indicates a subcritical flow, as discussed and put in general context with the diagram of possible flow regimes (Fig. 4.8).

	One Cusp (Fig. 4.1a)	Two Cusps (Fig. 4.1b)	Wave Train (Fig. 4.1c)
Time T [s]	2.2	2.6	3.2
Pulling Velocity V [cm/s]	41	56	60
Froude Number F	0.4	0.4	0.5
Wavelength of tail cusp λ [cm]	18	14	-
Amplitude of first cusp a [cm]	1.8	1.8	2.5

Table 4.1: Measured parameters in the gravity wave experiment

The trough develops further to a standing wave above the mountain with a horizontal wave length of 16 ± 1 cm and a tail of several cusps (Fig. 4.1b and 4.1c) moving towards the right (Tab. 4.1). The amplitude of the wave train decays from a maximum of 2.5 ± 0.1 cm relative to the mountain for the first wave to 0.5 ± 0.1 cm for the last wave, and resembles a damped harmonic buoyancy oscillation (Chapter 2). The tail of the wave is hard to follow, due to its rapid continuous development. The estimated tail speed of 19 ± 5 cm/s can only be an approximation and a larger error is involved compared to the pulling velocity. Nevertheless, the tail is clearly slower than the mountain.

In the atmosphere such steady waves are only possible (Smith 1979), when the phase velocity of the wave matches the mean flow speed (Eq. 4.4). Consequently, the magnitude of the pulling velocity must be equal to the phase velocity. The phase velocity (Eq. 4.2) is calculated from the dispersion relation (Eq. 4.1) for linear gravity waves (Cohen 2008) of finite depth (Landau & Lifschitz 1987) without surface tension (Grimshaw 2007). Here the phase velocity is not the typical shallow water wave speed, because $h \approx 2\lambda$ and therefore $\tan(kh) \approx 1$ where $k = 2\pi/\lambda$. The calculated average phase velocity of 50 ± 3 m/s is comparable to the average pulling velocity of 54 ± 1 cm/s. The dominating term in the calculated group velocity (Eq. 4.3) equals half that of the phase velocity. This leads to a dispersive effect apparent in the observation: the tailing wave cusps further to the right are

Linear Gravity Wave

Dispersion relation $\qquad \omega = \sqrt{gk \tanh(kh)} \qquad$ (Eq. 4.1)

Phase velocity $\qquad c_p = \dfrac{\omega}{k} \approx \sqrt{\dfrac{g}{k}} \qquad$ (Eq. 4.2)

Group velocity $\qquad c_g = \dfrac{\partial \omega}{\partial k} \approx \dfrac{1}{2}\sqrt{\dfrac{g}{k}} \qquad$ (Eq. 4.3)

Standing wave $\qquad c_n = -V \qquad$ (Eq. 4.4)

slower due to their shorter wave length (Fig. 4.1c, Tab. 4.1). The calculated group velocity of 25 ± 3 cm/s is a bit larger than the measured 19 ± 5 cm/s but within the error range.

As the Froude number increases due to faster pulling and a greater relative speed, the amplitude of the wave is observed to increase (Tab. 4.1). This effect can be explained by the continuity (Eq. 3.1) and Bernoulli equations (Eq. 3.2). When more water is flowing in less time over the obstacle, it has to flow faster. Blocking effects can be neglected here within the homogeneous layer (Baines 1995). Thus, potential energy is transferred into kinetic energy (Eq. 3.2). Faster fluid particles have more kinetic energy and less potential energy, which leads to a lower height of the water directly over the obstacle (Eq. 3.2) and an increase in wave amplitude (Fig. 4.1) from 1.8 to 2.5 cm (Tab. 4.1). In all gravity wave experiments mountain I produced the largest wave amplitudes due to its larger cross-sectional area.

The gravity wave experiment in the laboratory here can be compared to observations in the atmosphere (Chapter 2) and numerical simulations (Durran 2002, Smith 2002 and Chapter 6). Over the complex topography of the Mont Blanc mountain range a vertical cross section of the atmosphere could be recorded using backscatter Lidar techniques on the DLR Falcon plane (Smith, Volkert 2001). Horizontal wavelengths of 15 km and amplitudes of order 1 km were visible in the cloud patterns. In numerical simulations (Durran 2002) of an isolated mountain the waves had wave lengths of 10 km and amplitudes up to 4 km, which is comparable to the wavelength and amplitude observed in the laboratory when scaling km to cm. Due to the complex topography in the Alps the wave structure in the laboratory experiment is of course idealized.

Nonlinear advection, important for turbulent transport and eddy fluxes (Sprenger 2008) or finite amplitude wave effects (Chapter 6), have been neglected so far. Baines (1995) emphasized the importance of these features for certain flow regimes (section 4.5). Grimshaw (1986) simulated gravity waves including these effects with the Korteweg-de-Vries (KdV) equation (Fig. 4.2). Results can be a solitary or a cnoidal wave referred to as **undular bore** (Grimshaw 2007). In the simulation, the undular bore travels downstream as a wave train with decaying amplitude, as observed in the laboratory experiment here. Studying undular bores is a first step towards hydraulic jumps covered in the following section.
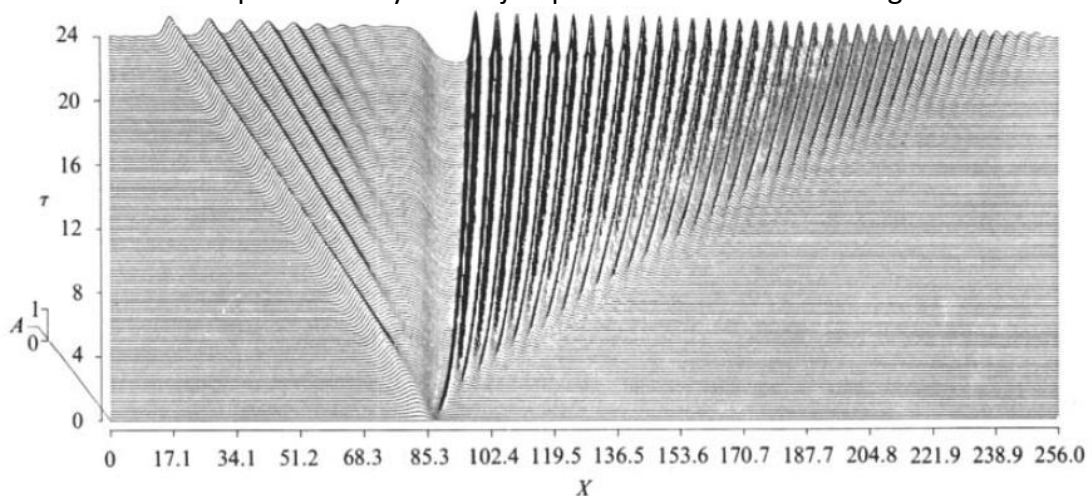
Fig. 4.2: Numerical simulation of the Korteweg-de-Vries equation showing a decaying undular bore downstream and an undamped bore upstream with a vertical time axis. (Grimshaw & Smyth 1986)

4.2   Hydraulic Jump

Hydraulic jumps occur in the atmosphere, oceans and rivers (Gohm 2008, Cohen 2008). A common example of a hydraulic jump is the roughly circular stationary wave that forms around the central stream of water in a sink. The jump is at the transition between the point, where the circle appears still and where the turbulence is visible. Opposed to continuous energy transformation like in an undular bore, turbulence is a characteristic of larger amplitude hydraulic jumps (Chapter 2), which are also referred to as turbulent bores (Simpson 1997). Pulling the mountain faster or decreasing water height transformed the undular bore seen in section 4.1 to a hydraulic jump.
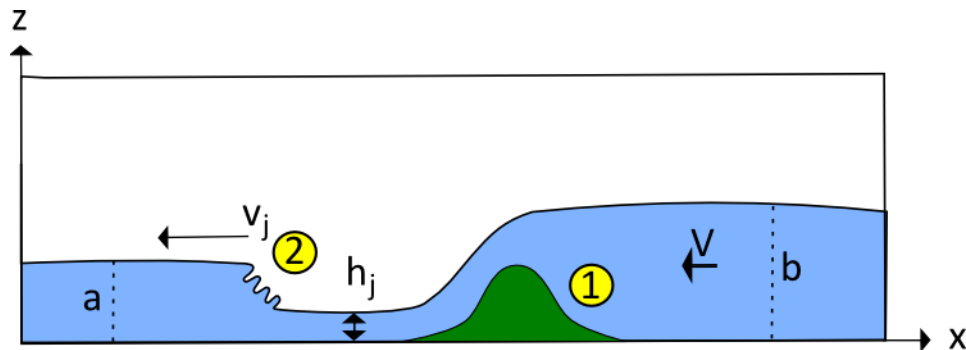
Fig. 4.3: Schematic of a propagating hydraulic jump (2) that evolved downstream and traveled away from the mountain (1) with velocity v_j, jump height h_j, two cross section (a) and (b).

The jump can be characterized by its jump height h_j and its velocity v_j (Fig. 4.4a). Furthermore, a cross section upstream (Fig. 4.3 - b) with water depth h_b and flow velocity v_b were compared to a cross section downstream (Fig. 4.3 - a) with water depth h_a and flow velocity v_a. In the experiment a propagating (Fig. 4.4a) and a stationary jump (Fig. 4.4b) were observed (Tab. 4.2).

Fig. 4.4a: Propagating hydraulic jump. Mountain is moving from left to right.
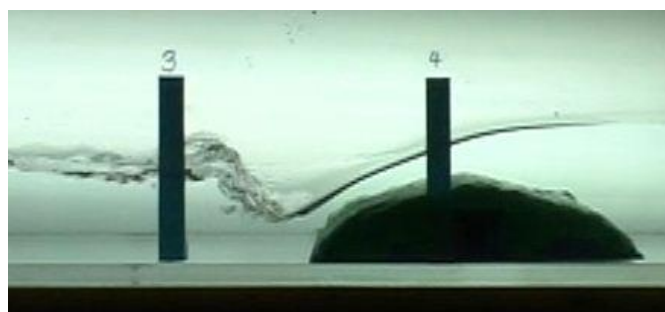
Fig. 4.4b: As in Fig. 4.4a but for a stationary jump. The mountain is moving slower than in Fig. 4.4a

The propagating jump (Fig. 4.4a) had a non dimensional speed between 0.1 and 0.3 (Tab. 4.2) downstream of the mountain. This is the speed of the hydraulic jump relatively to the shallow water velocity (Section 3.1). In the stationary jump case (Fig. 4.4b) $h_a/h_b = 0.5$ while in the propagating case $h_a/h_b = 0.4$ (Tab 4.2). The jump velocities match the expected calculated values (Baines 1995) further discussed in the flow regime diagram (Section 4.5). The jump heights are slightly below the theoretical values in the diagram due to measurement errors of h_a caused by a turbulent flow in the downstream cross section (Fig. 4.4) and variations in the Froude number, owing to not-constant pulling speed during the experiments (Excel Tables, DVD).

|	Propagating Jump (Fig. 4.4a)	Stationary Jump (Fig. 4.4b)
Froude Number F	0.7	0.4
Jump Speed	0.2	-
Jump height	0.4	0.5
Dissipated Energy ΔE [J/kg]	5.5	4.1

Table 4.2: Measured parameters in the hydraulic jump experiment. The non dimensional jump speed is defined as $vj/\sqrt{gh_a}$ and the relative jump height as h_j/h_a.

The flow evolution and development of the jumps can be described as follows. Water flows over the mountain and potential energy is transferred into kinetic energy (Fig. 4.4). The fluid speed can be calculated with the continuity equation (Eq. 4.5). Above the mountain at a critical water height h_c the flow velocity v_c was equal to the shallow water wave speed (Section 3.1). As the water flows downstream the mountain, it accelerates further to a **supercritical** state, where the fluid velocity is larger than the shallow water wave speed. This supercritical flow proceeds down the mountain slope and reaches the relatively slower fluid equal in velocity magnitude to the pulling speed V, which was below shallow water wave speed defined as **subcritical** flow (Landau & Lifschitz 1987). The rapid braking of the supercritical flow leads to turbulence in the jump region (Fig. 4.4). Using momentum conservation (Eq. 4.6) the dissipated kinetic energy (Eq. 4.7) could be calculated (Tab. 4.2) as in Cohen (2008) and was further analyzed in computer simulations (Chapter 6). Table 4.2 shows that more energy dissipated in the propagating jump.

Hydraulic Jump

Continuity Equation $\qquad Q = hv \equiv const$ (Eq. 4.5)

Momentum Conservation $\qquad \dfrac{1}{2}\rho g H_1^2 - \dfrac{1}{2}\rho g H_2^2 = \rho Q(v_2 - v_1)$ (Eq. 4.6)

Dissipated Energy $\qquad E_2 - E_1 = -(H_2 - H_1)\dfrac{g(H_2 - H_1)^2}{4H_1 H_2}$ (Eq. 4.7)

4.3   Blocking

Upstream effects for mountain flow due to blocking have been investigated in the laboratory (Long 1954, Baines 1987) and observed in the atmosphere (Smith 2005). Here, in the MIM laboratory blocking experiments were conducted with mountain I and mountain II. To generate a bore upstream, high Froude numbers above 1 were crucial (Tab. 4.3). A water depth of H = 3.0 ± 0.1 cm and an average pulling speed of V = 66 ± 1 cm/s were used. Under these conditions a transition (Tab. 4.3) between an undular bore (Fig. 4.5) and a turbulent hydraulic jump upstream could be observed comparable to Long's experiment (1954).
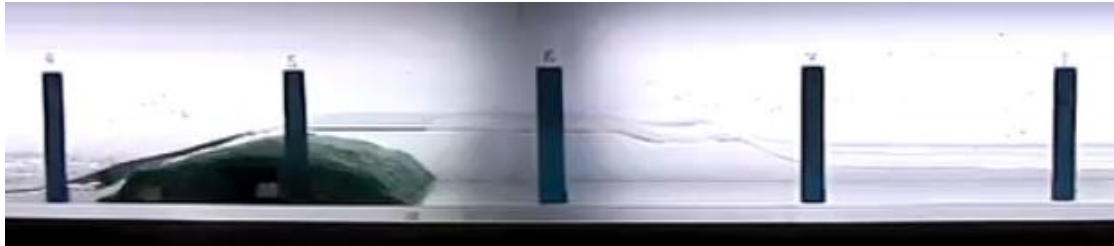
Fig. 4.5: Undular bore upstream. Mountain I is moving from left to right.

Initially water accumulates upstream of the mountain until an undular bore forms and travels upstream. A transition to a turbulent bore occurs when the Froude number is above 1.5 (Tab. 4.3). As described in Sprenger (2008) the Froude number is also an indicator for advection, which increases at higher Froude numbers. Obviously more water is advected at higher pulling speeds and kinetic energy of the fluid particles increases. The speed of the bore is above shallow water wave speed and increases further (Tab. 4.3). The energy transfer cannot occur with an undular bore anymore until it becomes turbulent.

Marker Position	Froude Number F	Flow Regime	Bore Speed
4	1.1	undular bore	1.4
5	1.2	undular bore	1.5
6	1.3	hydraulic jump	1.7

Table 4.3: Froude number, flow regime, and bore speed relative to the shallow water wave speed are listed when the mountain crosses the markers 4-7.

## 4.4   Supercritical Flow

Wave steepening and wave breaking are important concepts in the atmosphere (Smith 1977, 1979). They are nonlinear phenomena responsible for energy dissipation (Cohen 2008). In the laboratory wave braking (Fig. 4.6) was observed as well as supercritical flow (Fig. 4.7), which will be studied further in a two layer system (Chapter 5).
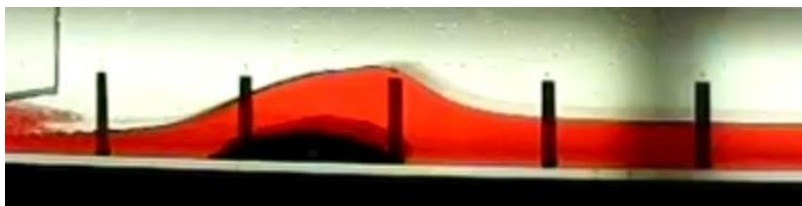
Fig. 4.6a: Partial blocking upstream.

Fig. 4.6b: Wave steepening.
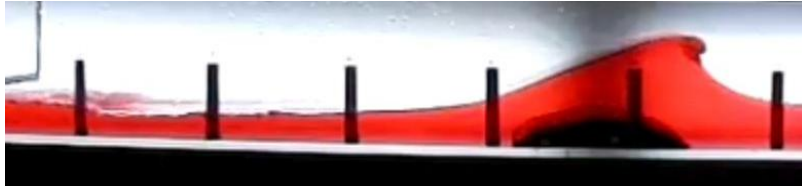
Fig. 4.6c: Initial wave breaking.

In this experiment mountain I was pulled with an average velocity of 145 ± 1 cm/s through water with an undisturbed depth of H = 6.1 ± 0.1 cm, which lead to a non dimensional mountain height h_m/H of 0.7. To have a better visible water surface, the water was colored red. A wavelength in size comparable to that of the obstacle (Smith 1979) indicates $H \ll \lambda$, in consequence the flow was non dispersive (Cohen 2008) and the wave did not spread. First partial blocking upstream the mountain was observed (Fig. 4.6a). While more water was advected, the wave began to steepen (Fig. 4.6b) and showed a typical shape described theoretically by Cohen (2008) until the wave began to break (Fig. 4.6c) at a relatively high Froude number (Tab. 4.4) and the energy dissipated into turbulence.

Marker Position	Froude Number F	Flow Regime
2	1.6	partial blocking
4	2.1	wave steepening
6	2.0	breaking

Table 4.4: Wave breaking at high Froude numbers.

One more experiment was conducted with the same water height, but a faster average speed of 260 ± 0.1 cm/s, which lead to a high Froude number of 3.4. Under these conditions a solitary wave (Fig. 4.7) above the mountain developed like in experiments by Baines (1987) and was also expected for a supercritical flow regime in the diagram (Fig. 4.8).

Fig. 4.7: Supercritical flow.

In the following section all experimental results will be compared to a general theory by Baines (1995) and plotted in a diagram (Fig. 4.8) of the possible flow regimes (Tab. 4.5).

17

4.5   Flow Regime Diagram

In this section the goal is to look back at the single layer experiments with a broader picture in mind (Tab. 4.5). A general analysis (Houghton & Kasahara 1968, Long 1954, Baines 1987 and 1995) of momentum conservation (Eq. 4.6), continuity (Eq. 3.1) and Bernoulli equation (Eq. 3.2) reveals the possible flow regimes in a diagram (Fig. 4.8). In numerical studies it was used by Smolarkiewicz (1996) and Wedi (2003). In operational forecasting the dependence of the flow regime on Froude number and mountain height might be useful to predict hazards like rotors (Chapter 2) for pilots.
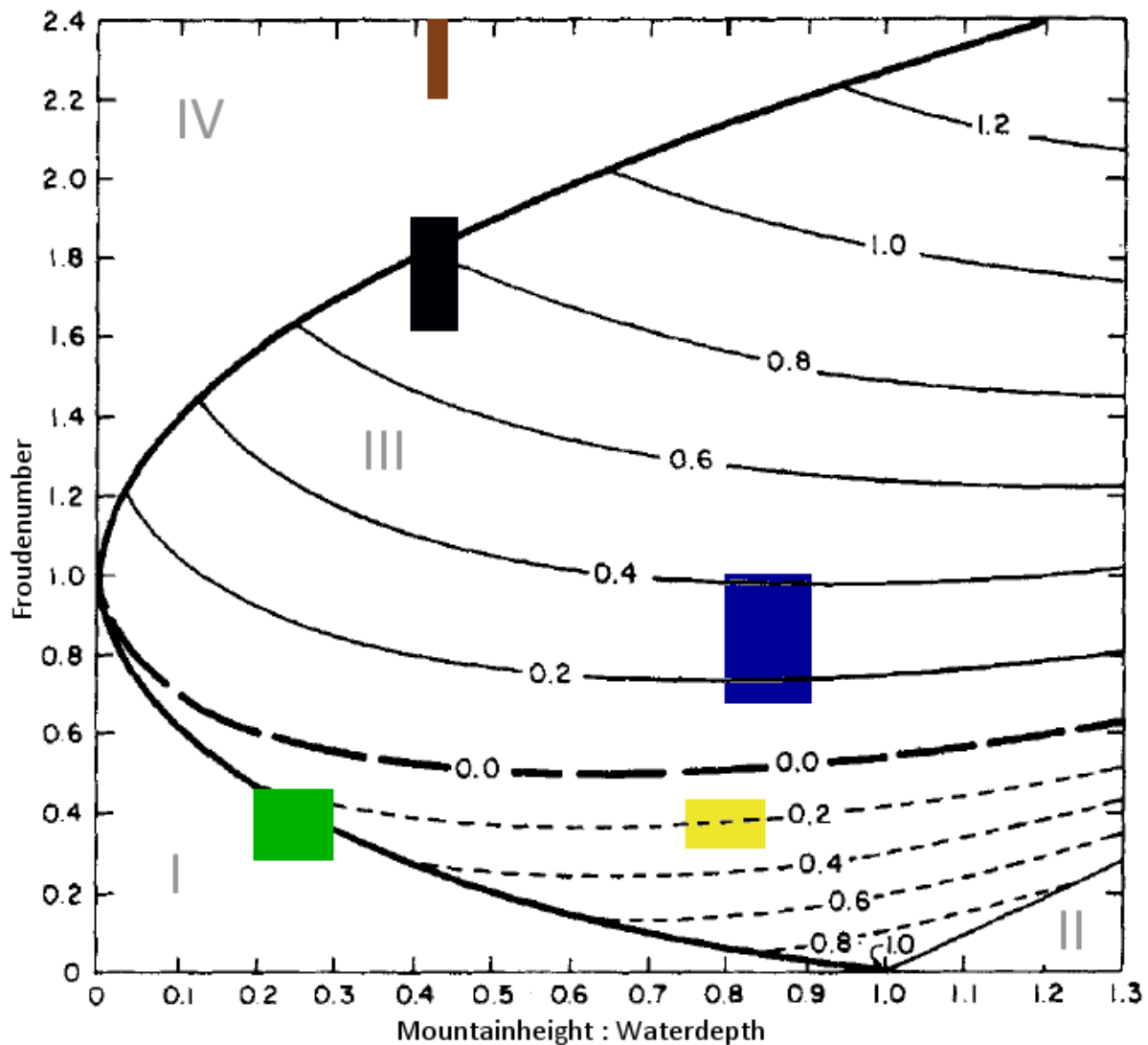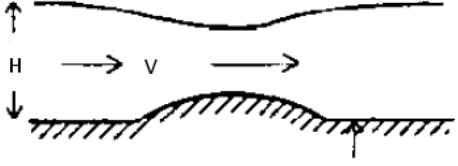

Fig. 4.8: Flow regime diagram (Houghton & Kasahara 1968). The flow strongly depends onFroude number (vertical axis) and non dimensional mountain height (horizontal axis). Basically four different flow regimes are present in this diagram: I) subcritical flow below the parabola, II) total blocking in the right triangle, III) partial blocking with hydraulic jumps inside the parabola, IV) supercritical flow in the white area above the parabola. Inside the parabola the solid lines indicate relative jump speed compared to shallow water velocity and the dashed lines show the position of a stationary jump compared to total mountain height. Each colored box represents the experiments presented in sections 4.1–4.4. For each experiment, a range of Froude numbers and non-dimensional heights is given, owing to non-constant pulling speed and blocking effects altering the fluid depth.

Besides the typical subcritical (Tab. 4.5 - I) and supercritical flows (Tab. 4.5 - IV) over an obstacle described for example by Landau & Lifschitz (1987), generally more flow regimes can be possibly differentiated further in the diagram above (Fig. 4.8). Schematically, the flow regimes were described by Baines (1995) and are presented in the following table:

I) subcritical flow Above a certain mountain height and Froude number a wave train is visible (Baines 1995) within the subcritical regime.	
II) total blocking Here a bore upstream of the obstacle develops. It can be undular or turbulent depending on Froude number.	
III) partial blocking & hydraulic jump The flow is blocked, a rarefaction (Baines 1987) develops upstream and a hydraulic jump forms downstream.	
IV) supercritical A solitary wave forms directly above the mountain.	

Tab. 4.5: Schematic of flow regimes by Baines (1995).

The experiments in the MIM laboratory here (Tab. 4.6) agree very well with the diagram (Fig. 4.8) and it was useful for adjusting Froude number and mountain height to show certain Föhn features (Chapter 2) like hydraulic jumps (Section 4.2) or lee waves (Section 4.1).

Box Color	Flow Regime	Section	Description
Green	I	4.1	Lee Wave
Yellow	II	4.2	Stationary Hydraulic Jump
Blue	II	4.2	Propagating Hydraulic Jump
Black	IV	4.4	Wave Steepening
Brown	IV	4.4	Supercritical Flow

Tab. 4.6: Experiments conducted in the MIM laboratory and presented in the diagram above.

The blocking experiment described in section 4.3 was outside the range plotted in Figure 4.8. It would be in the partial blocking area within the parabola with a downstream & upstream propagating hydraulic jump with center coordinates (height, Froude number) = (1.4, 1.2). The position of the stationary jump (Fig. 4.8 - Yellow Box) is a little bit overestimated. Due to

turbulence, the beginning of the hydraulic jump was hard to measure. Together with a slightly varying pulling velocity this might be the cause for the mismatch. The propagating jump (Fig. 4.8 - Blue Box) travels with a velocity between 0.1 and 0.3 (Tab. 4.2), which agrees well with the predicted velocity between 0.2 and 0.4 for the jump in the diagram (Fig. 4.8). Due to the inertia of the water, blocking effects reduce for higher flow velocities and thus for higher Froude numbers and supercritical flow. This explains why the non dimensional mountain height is sharper for supercritical flow (Fig. 4.8 - Brown Box).

Wind speed [m/s]	Critical Layer [km]	Froude number
80	4	0.4
40	3	0.2
20	10	0.1

Tab. 4.7: Maximum Froude numbers for a single layer.
The height of the fluid is determined by the critical layer.

Of course, the single layer system can only be a first approximation to the atmosphere. Long described the single layer as the troposphere (1954) before he studied multi layer systems and modeled a continuously stratified atmosphere (1955). Table 4.7 shows the Froude numbers expected for typical single-layer flows in Alpine regions for a mountain height of 5 km (Mont Blanc). As can be seen, the Froude numbers are at or below 0.4, meaning that only subcritical flow (Section 4.1), partial blocking (Section 4.2) with a stationary hydraulic jump and total blocking (Section 4.3) flows would be expected. Two layer systems, which are more similar to the atmosphere, are observed in the following Chapter.

5. Laboratory Results for a Two Layer Model

The vertical structure of the atmosphere is of course more complex than the model experiments in the laboratory presented in the previous Chapter. Only certain idealised configurations can be studied here which will allow an understanding of the more fundamental dynamics of flow over an obstacle. A vertical profile of the atmosphere above the Mont Blanc area during a Föhn event has been measured (Fig. 5.1) during the MAP campaign (Chapter 2). Wave structures were visible in the clouds and cloud parcel displacements (Smith 2002). Up to three homogeneous layers were observed in the vertical profile (Smith 2005). The next step in the laboratory model here is to use a two-layer fluid whose interface is comparable to a temperature inversion in the atmosphere, characteristic for observed Föhn events (Smith 2002, 2005). The interaction of an inversion with lee waves has been modeled numerically (Vosper 2006). Typically a temperature increase of order 2% occurs within the inversion layer (Smith 2005).
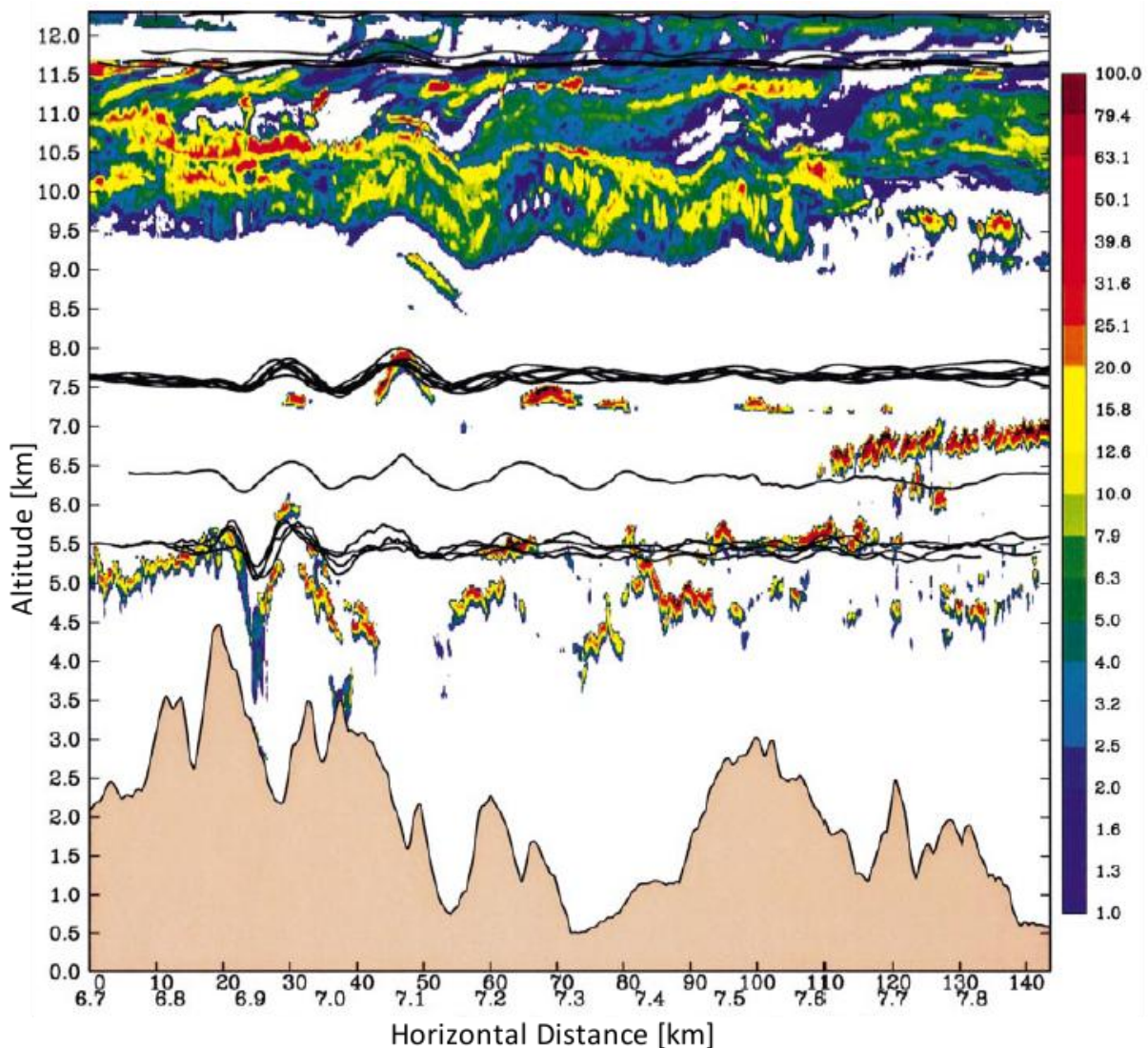
Fig. 5.1: Lidar backscatter profile over the Mont Blanc topography, taken from the DLR falcon. The color bar indicates optical thickness of the cloud. Also deeper clouds are visible below a strong cirrus layer. The black lines show calculated vertical displacements of cloud parcels (Smith 2002).

5.1 Nondimensional Parameters for a Two Layer Fluid

Not only can two layer systems be used to adequatly capture certain dynamics of the atmosphere, they also are observed in the ocean, for example when a cold river from a mountain glacier flows into the ocean water in a Fjord in Norway. When a boat travels over the water, the two fluids with a slightly different salt concentration interact and surface waves form on the layer separating the two fluids (Cohen 2008). In order to describe the two layer system appropriately it is necessary to introduce non dimensional variables as done for the single layer fluid (Chapter 3.1). This way, numerical simulations (Chapter 6) and observations (Chapter 2) from nature can be compared to laboratory studies.
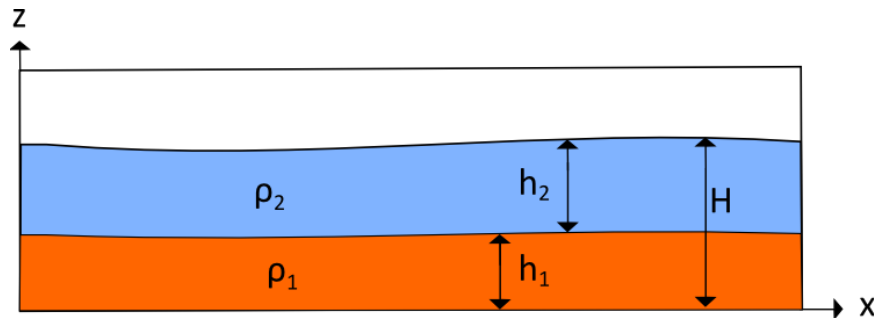

Fig. 5.2: Schematic of the two layer fluid. Each layer with density $\rho_{1/2}$, height $h_{1/2}$ and total fluid height $H=h_1+h_2$.

As in Baines (1987, 1995) a Froude number will be defined similar to the one in the single layer system. Furthermore a Blocking number (Baines 1987) also referred to as inverse Froude number F_i (Sprenger 2008) which depends on Brunt Väisälä frequency N, mountain height h_m and flow velocity V is used here. The Brunt Väisälä frequency depends on stratification, which is the gradient of the density profile and gravity. Here, $\rho(z)$ is the density which is a function of height, z is the vertical coordinate, and ρ_0 a reference density on the bottom of the tank where $z = 0$. The shallow water velocity for linear waves V0 is different compared to the single layer system (Chapter 3.1) due to the density difference with the overlying fluid being lower. To allow different heights of the two layers, h_1 is the height of the lower layer and h_2 the height of the top layer. Finally, the density in the lower layer is ρ_1 and in the top layer it is ρ_2 (Fig. 5.2).

Important Quantities for the Two Layer Fluid

|			
Froude number	$Fr = \dfrac{V}{V_0}$	Blocking number	$F_i = \dfrac{Nh_m}{V}$
Shallow water velocity	$V_0^2 = \dfrac{g(\rho_1 - \rho_2)}{\dfrac{\rho_1}{h_1} + \dfrac{\rho_2}{h_2}}$	Buoyancy	$g' = g\dfrac{\rho_1 - \rho_2}{\rho_0}$
Brunt Väisälä frequency	$N = \sqrt{\dfrac{g}{\rho_0}\dfrac{\partial \rho}{\partial z}}$		

5.2   Experiment Setup

The two layer model provides the possibility to study lee waves and hydraulic jumps as before, but compared to the single layer flow, the motions will appear in slow motion for the observer (Simpson 1997). The acceleration due to gravity decreases and the Froude number changes. For simplicity reasons it is convenient to look at a two layer system with two layers each of height h (Baines 1987). In this case the flow diagram shown in Fig. 4.8 is modified (Section 5.3). Possibly, finite amplitude effects can be observed (Baines 1995), like amplitude growth for certain flow velocities, typical for nonlinear waves (Goler 2004).

Experiments examining flow over an obstacle in a two layer fluid have been conducted by Long (1954). He suggested using salt and tap water, whose density difference would be closer to that observed in the atmosphere than the fluids he used. Furthermore, the salt water can be colored with food coloring and is no harm for the environment and the students during the experiment.

First, two methods to create a stable two layer fluid in the tank will be addressed here: a gravity current (Fig. 5.5) to produce the denser layer (Simpson 1997), or a controlled release of the denser fluid using a hose at the bottom of the tank (Fig. 5.3). The advantage of the first method is that it requires less time to set up than for the second method. Both methods will be implemented here to examine which one provides results consistent with those of Baines (1995.)

To produce the stable layer using a controlled release of the denser fluid, the tank is first filled with water. The volume of the stable layer is calculated based on the dimensions of the tank (Chapter 3), and the required density produced by adding a sufficient amount of salt along with the food coloring. This fluid for the denser layer is mixed in a large bucket.

Next, the salt water is poured into a smaller container on the tank (Fig. 5.3 - 1) which has a tap (Fig. 5.3 - 2) with a hose (Fig. 5.3 - 3) attached to the bottom of the tank. The tap allows the rate of flow to be regulated. To minimize the turbulent mixing between the inflowing salt water and the water, a mean flow rate of half a liter per minute
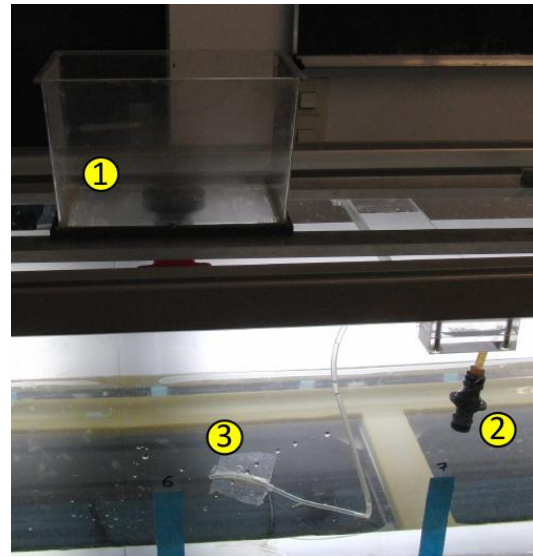
Fig. 5.3: Container (1) set on top of the tank. A little hose is fixed on the tank bottom (3) and connected to the container with a tap (2).

Fig. 5.4: Turbulent mixing of salt water from the hose, which slowly sets on the tank bottom with tap water above.
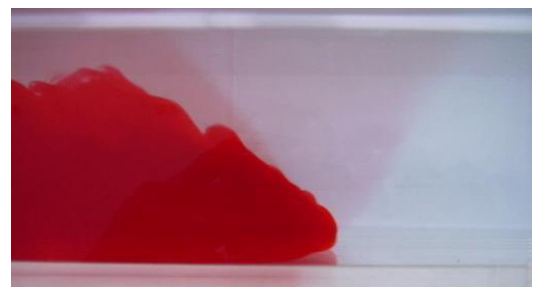
Fig. 5.5: Gravity current – red colored salt water is propagating into the lighter tap water from left to right.

is used here, slower at the beginning and a little faster as the depth of the dense layer increases.

The turbulent mixing (Fig. 5.4) occurs through Kelvin Helmholtz instability, especially at the beginning, when the bottom layer is very thin.

Diffusion, which acts on longer time scales, occurs as the denser fluid spreads slowly along the tank bottom reaching the ends of the tank. The effect of diffusion can be seen in the following example. The stable layer has a density 2% greater than that of water. After the dense layer (colored red) reached a height of 2 cm, the height of both layers is measured every 20 minutes (Fig. 5.6). The mixing produced a much thicker red layer than expected. With 16 liters of salt water the red layer should be about 2.5 cm high in the end. However, in the experiment it reached, due to diffusion, a height of 4 cm (see Fig. 5.6).

In order to produce the stable layer using a gravity current, tap water is filled into the entire tank up to a height of 7.5 cm. At 1/3 of the tank length a dam wall is installed and the necessary amount of salt (28.5 g/liter) is added along with some food coloring into the smaller part of the tank. After mixing the fluid with a wooden spoon to dissolve the salt and then letting the water settle, the separating wall is lifted up quickly. A gravity current (Fig. 5.5) travels to the other side of the tank within 30s, internal surface waves (Cohen 2008) form due to reflection of the gravity current at the tank wall until equilibrium is reached after 5 min.

Fig. 5.6: Height of the red layer every 20 minutes. The black shows the total water height H. Red dots indicate the height of the denser layer on the left side and red dashes for the right side. The red line shows the ideal red layer height at each timestep without mixing.
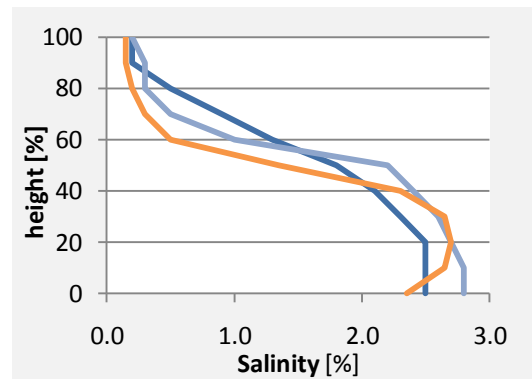
Fig. 5.7: Density profile from the bottom of the tank until salinity approaches 0%. The dark blue line shows the profile after filling denser fluid slowly into the tank with the hose. Orange is the average profile between left and right side after an equilibrium stable layer formed after the gravity current. The light blue line shows the profile of the gravity current after 5 experiments have been conducted.

Compared to the time consuming method before, which used up more than 2 hours, the gravity current is much quicker and less turbulent diffusion takes place (Fig. 5.7). The density profile is a lot sharper, even after the pulling experiments have been conducted.
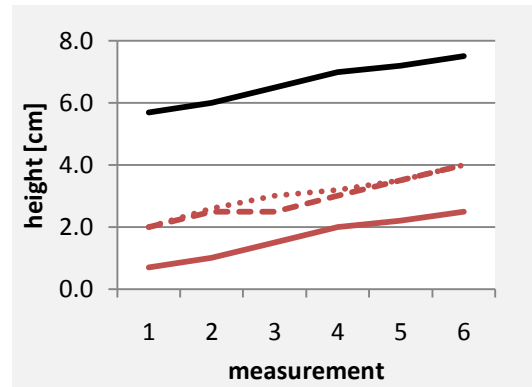
5.3 Two Layer Results

Similar Föhn features can be reproduced as for the single layer system (Baines 1995). In the MIM experiments non linear effects like wave amplification (Goler 2004), only visible in this two layer system (Baines 1987) were the focus of the observations in this section.
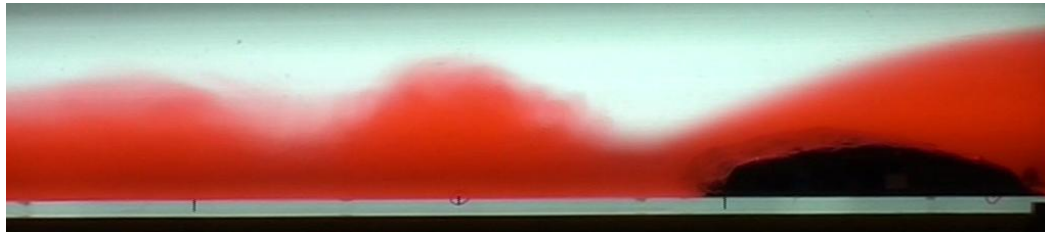
Fig. 5.8: Amplifying lee wave when mountain is pulled from left to right.

*Fig. 5.9: Wave dissipation, when the mountain is pulled to the left quickly.*

For waves travelling with the same speed as the mountain a growth in amplitude over time is anticipated (Goler 2004). To validate this, the mountain is first pulled quickly with a speed of 10 cm/s, where lee wave forms (Etling, 2010). After the first wave cusp is visible, the mountain is pulled at a speed comparable to the travelling wave speed of about 4 cm/s, which is of order 10 smaller than in the single layer experiment. The reason is the reduced gravitational acceleration within the two layer system. Through turbulent feedback, the wave becomes more apparent (Fig. 5.8) and also increases in amplitude (Fig. 5.10) as anticipated for this velocity. This effect is similar to resonance in classical mechanics, where amplification occurs only for certain frequencies in an oscillating system. In contrast to the single layer experiment, the wave is now neither laminar nor turbulent, but dominated by both effects.

If the mountain is pulled faster than the wave velocity, the wave cusp widens (Fig 5.9). In one case the wave has a constant velocity of 5 cm/s, while the mountain has an average velocity of 7 cm/s. The wave amplitude is smaller and the wavelength larger than in the experiment before, where mountain pulling speed and wave velocity coincided. The wave structure is more laminar. The further the wave travels thus becoming further separated from the mountain, the more it dissipates. The two experiments show the processes of wave dissipation (Fig. 5.9) and steepening (Fig. 5.8). Measuring the wavelength of the trailing cusps in both experiments, which decreases, shows the dispersive effect already
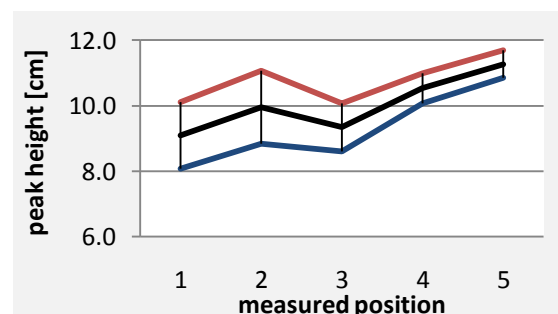
Fig. 5.10: Growth of the first wave peak measured every 10 cm. The red line indicates the maximum height of the measurement, the blue line the minimum measured height and the black line the arithmetic mean. The measurement error becomes smaller over time and the interface sharper as the wave develops further.

observed for a single layer (Chapter 4.1). Wave steepening, dissipation and dispersion determine the development of a wave (Baines 1987).

For lower velocities of the mountain a hydraulic jump forms (Fig. 5.11, Fig. 5.12) in the lee of the mountain as discussed with numerical and laboratory experiments by Etling (2010). In the experiments here, partial blocking and supercritical flow have been covered for a Froude number between 0.3 and 0.8 and a non dimensional mountain height of 0.3. The results agree well with diagrams by Baines (Fig. 5.12) and Etling (Fig. 5.11) for a two layer fluid with two equally high layers, where both rotors and lee waves are possible in this partial blocking regime.

In Baines diagram (Fig. 5.12) only flow with a non dimensional mountain height below 0.5 is possible for the Alps, if the upper layer represents the top of the troposphere up to about 10 km, the interface at about 5 km to have two equally high layers, and a maximum mountain height of about 5 km in the Alps. In the experiments presented here only Froude numbers below 1 were covered with pulling velocities below 10 cm/s. By increasing the velocity, a supercritical flow with a Froude number above 1 can easily be simulated. A lower pulling velocity is necessary than in the single layer experiments (Section 4.4). Supercritical flow can occur in the Alps (Tab. 4.8).

Additional experiments have been performed with a range of layer depths and a smaller mountain, and these are presented in the attached DVD. These experiments highlight supercritical flows and upstream propagating bores. A 3-layer experiment was also performed and shown in the DVD (Fig. 5.13). However, to interpret these experiments quantitatively, many experiments would be necessary. And as each experiment requires about 1-2 kg of salt, this was not feasible, and so the videos are retained, but the results not presented herein. Furthermore, during the summer semester students' laboratory, where usually 10 groups participate, an inappropriately large amount of salt between 10–20 kg would be necessary.
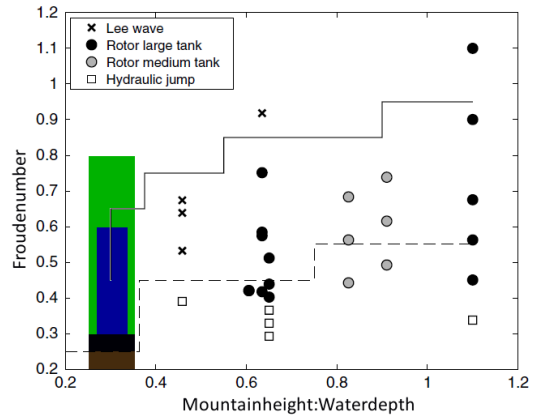

Fig. 5.11: The lines separate flow regimes as obtained in the numerical simulations of Vosper (2004): lee waves from rotors (solid line), and rotors from hydraulic jumps (dashed line). The green box shows the first experiment (Fig. 5.8). The smaller blue box is for the second experiment (Fig. 5.9). Brown and black are subcritical flow experiments (DVD).
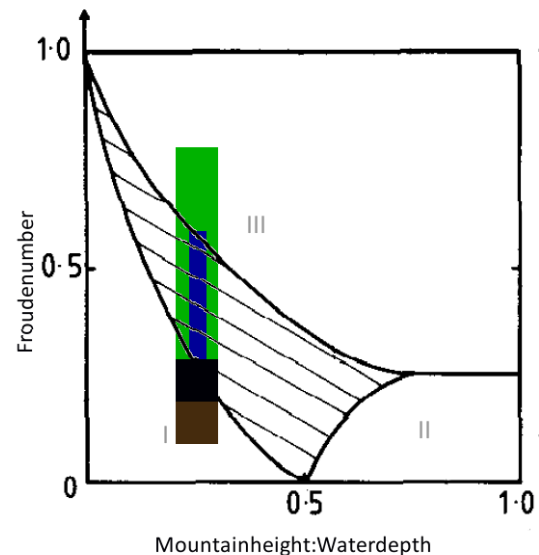

Fig. 5.12: Flow regime diagram by Baines (1987) for two layers with the same height. I) Subcritical flow, II) Total blocking, III & shaded area) partial blocking. The green box shows again the first experiment and the blue box the second one. Brown and black show subcritical flow experiments (DVD).
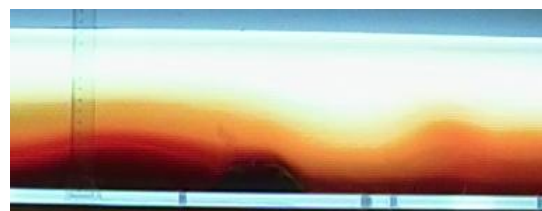
Fig. 5.13: First multi layer experiments with a small mountain.

Wind speed [m/s]	Critical Layer [km]	Froude number
80	4	2.8
40	3	1.6
20	10	0.5

Tab. 5.1: Maximum Froude numbers for a two layer system.
The height of the fluid is determined by the critical layer.

Table 5.1 shows the Froude numbers expected for typical two-layer flows in Alpine regions for a mountain height of 5 km (Mont Blanc). Due to the use of the reduced gravity in the Froude number, large Froude numbers are permitted compared with the single-layer experiments in Chapter 4. This means that all flow regimes would be expected to occur.

6. Numerical Simulations of the Föhn in a Tank

To examine the experiment from another point of view, numerical simulations are conducted and presented herein, which can be repeated with changes to parameters like pulling velocity and critical layer height. Eulag, a geophysical flow model is used, which can handle laboratory scales of mm as well as large meteorological scales (Prusa 2007). Flows over an obstacle with a single layer have already been conducted by Wedi & Smolarkiewicz (2003). Here, the two layer experiment is modeled with an inversion layer (Vosper 2006, Etling 2010) as in the laboratory. This simulation is included in the students' tutorial (Appendix A) to motivate the use of computer simulations and improve their understanding with the background knowledge of a similar laboratory experiment (Chapter 3-5) that they have already conducted.
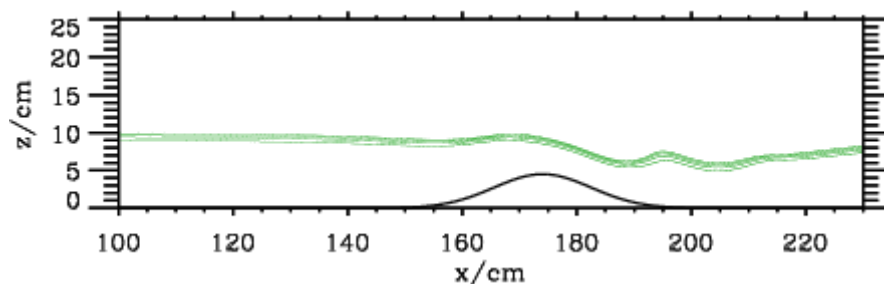
Fig. 6.1a: Numerical simulation of a two-layer flow over a hill. A first wave cusp is visible, after 1.2s.
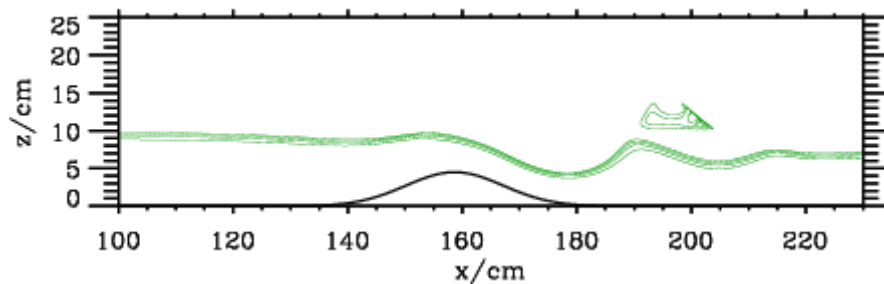
Fig. 6.1b: After 1.8s a second cusp forms.
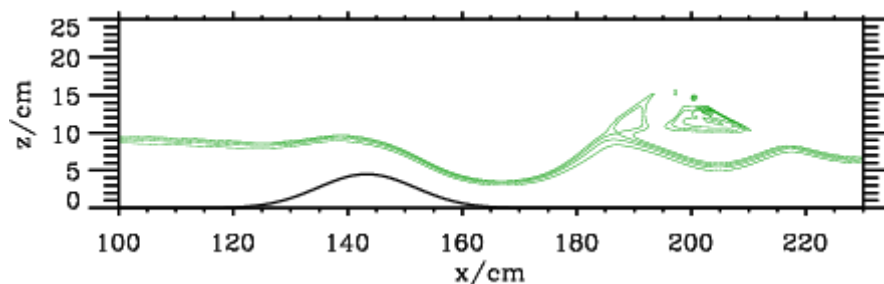
Fig. 6.1c: The wave clearly amplified after 2.4s.

The simulation is set up in two-dimensions with a grid resolution of 1 mm and the size of the tank as specified in Chapter 3. An absorbing sponge is introduced above 20 cm in the vertical and at the ends of the tank. A Gaussian shape mountain is used with a full width at half maximum comparable to the mountain in the two layer experiment. The lower boundary with the topography is time dependent, so that the mountain could move. Using the parabolic shape of the mountain in the experiment lead to difficulties at the foot of the mountain, because the topography function needs to be smooth and differentiable in every point.

Two different background profiles of the potential temperature for water are used, the first having an inversion (Fig. 6.1) and the second a continuous stratification (Fig. 6.2). The green lines are a passive scalar, initialized with the potential temperature field. In the two layer simulation, the potential temperature is 10 % smaller in the lower layer than above the inversion. A critical layer thickness of 5 cm lead to a Brunt Väisälä frequency of $N=4$ s^{-1}. Compared to the laboratory model, where $N=2$ s^{-1}, the critical layer in the simulation is more stable. To have similar Froude numbers and wave velocities (Chapter 5.1), the velocities have to be adjusted to the greater potential temperature difference. The scaling factor is $2.2=\sqrt{10\%}/\sqrt{2\%}$. In the simulation the mountain moves quicker than the wave and it is also moving quicker relative to the mountain in the laboratory experiments (Fig. 5.8, Fig. 5.9). In the two layer simulation shown in Fig. 6.1 the mountain moves to the left with a velocity of 25 cm/s a background flow with 5cm/s to the right lead to a total velocity between fluid and mountain of 30 cm/s. A background flow is introduced to reduce the speed of the mountain and thus make the flow more laminar.

After 1.2 s (Fig. 6.1a) a single wave cusp forms in the two layer simulation. The second cusp becomes visible in Fig. 6.1b. After 2.4 s (Fig. 6.1c) the wave clearly amplifies and the distance between mountain and wave increases further. A closed loop of passive tracer above the wave indicates a rotor (Fig. 6.1b) in the neutral layer above the inversion. This is one problem with the two neutral layers separated by an inversion in the laboratory experiment as well, as in the numerical simulation. Initially small turbulent eddies form in the shear layer, subsequently amplify and grow within the neutral layer, leading to mixing between the two layers. To find out the right parameters for the two layer experiments (Fig. 5.8 and Fig. 5.9), the simulations provided good assistance.
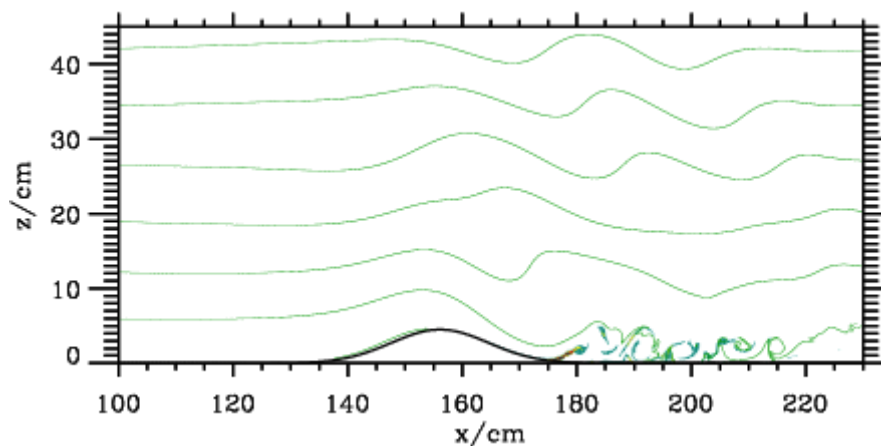
Fig. 6.2: As in Fig. 6.1 but for a continuously stratified fluid with the mountain moving from right to left.

The continuously stratified model (Fig. 6.2) is simulated with fewer processors and is quicker than the two layer model (Tab. 6.1). It can also be set up on a personal computer and run serially for the students' laboratory (Andreas Dörnbrack, personal communications). In the hydraulic jump region right of the mountain, the shading shows turbulent kinetic energy. Above a height of 20 cm gravity wave development is clearly visible. A phase shift between the lee waves at different heights can be observed.

A numerical model solves the necessary equations of motion. For flow over an obstacle, the shallow water equations can be used (Erhardt 2007), the anelastic equations (Prusa 2007) used here, or the more sophisticated Korteweg-de Vries (KdV) equation (Grimshaw 2007). Depending on which equations are used for the flow, the model output is different (Smolarkiewicz 1996). In consequence there is no perfect numerical model. They are approximations to reality and only in combination with laboratory studies (Chapter 3-5) and real world observations (Chapter 2) do they increase the understanding.

	Two Layer Model	**Stratified**	**Stratified**
Computational Time	6h, 50min	7h, 20min	1min
Number of Processors	128	64	64
Resolution	1 mm	1mm	1cm
Model time	3s	20s	30s

Tab. 6.1: Computational Time, Processors and Resolution on DKRZ Supercomputer.

Conclusions

The aim of this work has been to develop an experiment in the MIM laboratory to investigate the dynamics of the Föhn. First, a number of Föhn theories are presented. The hydraulic Föhn theory (Schweitzer 1953), which covers many of the Föhn features, like gravity waves, hydraulic jumps, and blocking effects discussed in Chapter 2, is the basis for this thesis and the laboratory experiments. These features are often made visible by lenticular clouds, cloud lines or rotor clouds in the atmosphere.

To understand the hydraulic Föhn theory and the basic fluid mechanics (Long 1953) of the flow over a mountain, which is responisble for the shape of these clouds, a simple laboratory experiment is set up in Chapter 3 for the students. The basic idea is that the flow of air over a mountain in the atmosphere can be shown to be similar to the flow of water over a moving obstacle in the laboratory (Section 3.1).

Improvements can be done concerning the pulling mechanism of the mountain (Section 3.3) in the experiment, which often leads to non-constant pulling speeds (Section 4.5). Other than that, the modelling clay, the simple set up of the mountain on a lego plate proved to be flexible and offers good results (Chapter 4) that show the basic Föhn features which can be compared to a general theory by Baines (Section 4.5). Single layer experiments (Chapter 3-4) have been the focus of this thesis.

More complex experiments are presented in Chapter 5, where a two layer fluid is set up. The interface between the two fluids (Section 5.2) is comparable to an inversion in the atmosphere, where gravity waves form (Smith 2006). The best and quickest method to set up this two layer system has been shown to be done using a gravity current (Section 5.2). In future work, more experiments can be conducted, to cover a number of flow regimes (Section 5.3) and different critical layer heights. However, with a density difference of only 2% and two neutral layers above each other, the interface is still less stable than in experiments by Long (1954) or Etling (2010).

In the end, a simulation of the laboratory experiments with Eulag (Chapter 6) is presented. It can be a basis for student experiments on the computer (Appendix A) to study the flow over a mountain from another point of view. To run it on a university computer, a serial code can be set up. A DVD with films (Appendix B) of the laboratory experiments has been created and can be used for teaching purposes.

Hopefully the new experiment presented in Appendix A can become part of the students' laboratory to increase the understanding for mountain meteorology and the analogies in physics. It seems impressive, how much the flow in the Eisbach in Munich has in common with the Föhn in the Alps.

Appendix

A) Laboratory Tutorial for the Students

A short extract from the Students' Laboratory Tutorial:

Um Alpen und Labor vergleichen zu können bestimmen Sie die Froudezahl F = $v/\sqrt{gh}$ bei bestimmten Strömungsverhältnissen und passen die Laborbedingungen entsprechend an!

1 Schicht	Alpen	Labor
Geschwindigkeit	30 m/s	30 cm/s
Höhe der Inversion	4 km	?
Froudezahl	0.2	0.2

Labor Experiment

Setzen Sie den vorgefertigten Berg aus Plastilin in den Tank. Befestigen Sie die Schnüre und die Halterungen wie folgt:
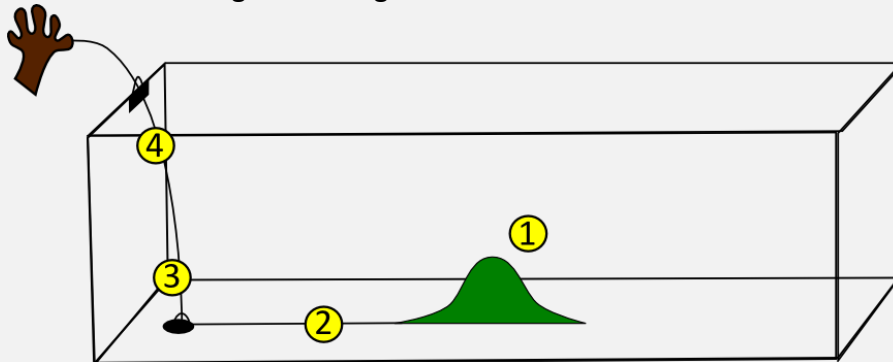
(1) Berg, (2) Drachenschnur, (3) Saughaken, und(4)Schraubhalterung.

- Die Befestigung wird auf beiden Seiten des Tanks angebracht und auf beide Seiten geht jeweils eine Drachenschnur vom Berg weg.
- Füllen Sie nun den Tank bis zu der berechneten Höhe. Es sollte ein Versuch bei 18 cm und einer mit etwa 6 cm Wasserhöhe durchgeführt werden.

Simulation am Computer

Der Versuch wird im Computer nachgestellt. Rufen Sie dazu das **Eulag** Programm auf. Dort können Sie Windgeschwindigkeit *u00* und Berg Höhe *amp* beliebig anpassen. Ihr **Tutor** hilft Ihnen beim Ausführen des Programms! Was beobachten Sie in geringer Höhe, was in großer Höhe? Welche Erklärung gibt es dafür und wie passt es zu den Laborergebnissen?

Connecting the Dots

- Wie entsteht eine Lenticularis Wolke, wie eine Föhnmauer?
- Berechne die Froudezahl für die Strömung im Eisbach!

B) Föhn Experiment Videos

This is the DVD menu with clips of the experiments:

Bibliography

Mountain Waves

Baines, Peter G., 1987: Upstream Blocking and Airflow over Mountains. *Ann. Rev. Fluid Mech.*, **19**, 75-97

Baines, Peter G., 1995: Topographic Effects in Stratified Flows. *Cambridge Monographs on Mechanics*, Cambridge University Press

Cohen, Ira M., and Pijush K. Kundu, 2008: Fluid Mechanics. *Academic Press*, Elsevier, 213-294

Dörnbrack, A., R. Heise, and J. P. Kuettner, 2006: Wellen und Rotoren. Atmosphäre und Gebirge, *Promet*, **1/2**, 1-24

Doyle, James D., and Dale R. Durran, 2002: The Dynamics of Mountain-Wave-Induced Rotors. *J. Atmos. Sci.*, **59**, 186-201

Frey, K., 1944: Zur Entwicklung des Föhns. *Verh. Schweiz. Naturforsch. Ges.*, 90

Frey, K., 1953: Die Entwicklung des Süd- und des Nordföhns. *Arch. Met. Geoph. Biocl.*, **5**, 432-477

Grimshaw R.H.J., 1986, and N. Smyth: Resonant flow of a stratified fluid over topography. *J. Fluid Mech.*, **169**, 429-464

Grimshaw, R. H. J., 2007: Solitary Waves in Fluids. *Intern. Series on Adv. in Fluid Mech.*, WITpress, 19-53

Gohm, A. and G.J. Mayr, 2004: Hydraulic aspects of föhn winds in an Alpine valley. *Q.J.R. Meteorol. Soc.*, **130**, 449 – 480

Gohm, A., G. J. Mayr, A. Fix, and A. Giez, 2008: On the onset of bora and the formation of rotors and jumps near a mountain gap. *Q. J. R. Meteorol. Soc.*, **134**, 21-46

Goler, R. A., and M. J. Reeder, 2004: The generation of the morning glory. *J. Atmos. Sci.*, **61**, 1360-1376.

Houghton, David D., and Akira Kasahara, 1968: Nonlinear Shallow Fluid Flow Over an Isolated Ridge. *Comm. on Pure and Appl. Math.*, **XXI**, 1-23

Küttner, 1939: Zur Entstehung der Föhnwelle. *Beitr. zur Physik der freien Atmos.*, **25**, 251-299

Jiang, Q., J.D. Doyle, and R. B. Smith, 2005: Blocking , descent and gravity waves: Observations and modelling of a MAP northerly föhn event. *Q. J. R. Meteorol. Soc.,* **131**, 675–701

Landau, L. D., and E. M. Lifshitz, 1987: Fluid Mechanics. *Volume 6 of Course of Theoretical Physics*, Butterworth-Heinemann, 31 pp.

Long, 1953: Some Aspects of the Flow of Stratified Fluids. I) A Theoretical Investigation. *Tellus*, **5**, 42-58

Long, 1954: Some Aspects of the Flow of Stratified Fluids. II) Experiments with a Two-Fluid System. *Tellus*, **6**, 97-115

Long, 1955: Some Aspects of the Flow of Stratified Fluids. III) Continuous Density Gradient. *Tellus*, **7**, 341-357

Mayr, G. J., L. Armi, S. Arnold, R. M. Banta, L. S. Darby, D. D. Durran, C. Flamant, S. Gaberšek, A. Gohm and R. Mayr, et al., 2004: Gap flow measurements during the Mesoscale Alpine Program. *Meteorol. and Atmos. Physics*, **86**, 1-2, 99-119

Mayr, G. J., and A. Gohm: Schnelle Strömungen durch Gebirgseinschnitte. Atmosphäre und Gebirge, *Promet*, **1/2**, 11-17

Schweitzer, H., 1953: Versuch einer Erklärung des Föhns als Luftströmung mit überkritischer Geschwindigkeit. *Archiv Met. Geo. Biokl.*, **5**, 350-371

Seibert, P., 1999: South föhn studies since the ALPEX Experiment. *Meteorol. and Atmos. Physics.* **43**, 91–103

Simpson, John E., 1997: Gravity Currents in the Environment and the Laboratory. Cambridge University Press, 5-9

Smith, R. B., 1977: The Steepening of Hydrostatic Mountain Waves. *J. Atmos. Sci.*, **34**, 1634-1654

Smith, R. B., 1979: The Influence of Mountains on the Atmosphere. *Advances in Geophysics*, **21**, 87-230

Smith, R. B., S. Skubis, J. D. Doyle, A. S. Broad, C. Kiemle, and H. Volkert, 2002: Mountain Waves over Mont Blanc: Influence of a Stagnant Boundary Layer. *J. Atmos. Sci.*, **59**, 2073–2092

Steinacker, R., 2006: Alpiner Föhn – eine neue Strophe zu einem alten Lied. Atmosphäre und Gebirge, *Promet*, **1/2**, 3-10

Numerical Modelling

Knigge، C., D. Etling, A. Paci, O. Eiff, 2010: Laboratory experiments on mountain-induced rotors. *Q. J. R. Meteorol. Soc.,* **136**, 442–450

Erhardt, 2007: Numerische Lösung der Flachwassergleichung mit Hilfe der Methode der Finiten Massen. Dissertation, LMU Munich: Department of Physics

Nadiga, B. T. , L. G. Margolin, and Piotr K. Smolarkiewicz, 1996: Different approximations of shallow fluid flow over an obstacle. *Phys. Fluids*, **8**, 2066-2077

Prusa, Joseph M., Piotr K. Smolarkiewicz, and Andrzej A. Wyszogrodzk, 2007: EULAG, a computational model for multiscale flows. *Computer & Fluids*, **37**, 1193-1207

Vosper, S.B., 2006: Inversion effects on mountain lee waves. *Q. J. R. Meteorol. Soc.,* **130**, 1723–1748

Wedi, N. P., and P. K. Smolarkiewicz (2004). Extending Gal-Chen & Somerville terrain-following coordinate transformation on time-dependent curvilinear boundaries. *J. Comput. Phys.*, **193**, 1–20.

University Lectures

Goler, R. A., 2009: Synoptik – Föhn. *LMU*

Illari, L., J. Marshall, P. Bannon, S. Lee, R. Najjar, J. Botella, R. Clark, A. Kumar, T. Sikora, T. Haine, K. J. Mackin, G. A. McKinley, M. Morgan, and A. Tandon, 2009: "Weather in a Tank"—Exploiting Laboratory Experiments in the Teaching of Meteorology, Oceanography, and Climate. *Bulletin of the American Meteorological Society*, **90**, 1619–1632

Lesch, H., and H. Zohm, 2009: T6 - Theoretische Hydrondynamik. *LMU*

Sprenger, Michael, 2008: Mesoskalige Dynamik – Gebirge. *ETH*

Spangler, 2004: Mountain Waves and Downslope Winds. Meted Program, *UCAR*